

Strain-engineered anisotropic conductance enhancement in corrugated monolayer MoS_2

Yimai Jiang(蒋伊麦), Jianing Tan(谭家宁), Meng Ge(葛蒙), and Gang Ouyang(欧阳钢)
Citation: Chin. Phys. B, 2026, 35 (**4**): 047701. DOI: 10.1088/1674-1056/ae0d59
http://cpb.iphy.ac.cn; http://iopscience.iop.org/cpb

What follows is a list of articles you may be interested in

Design of electrocaloric materials based on *E-T* phase diagrams

Fei Han(韩飞), Rongju Zhong(钟容菊), Jikun Yang(杨继昆), Chuanbao Liu(刘传宝), and Yang Bai(白洋)
Chin. Phys. B, 2026, 35 (**2**): 027704. DOI: 10.1088/1674-1056/ae3308

Ferroelectricity induced by the absorption of water molecules on double helix SnIP

Dan Liu(刘聃), Ran Wei(魏冉), Lin Han(韩琳), Chen Zhu(朱琛), and Shuai Dong(董帅)
Chin. Phys. B, 2023, 32 (**3**): 037701. DOI: 10.1088/1674-1056/ac7f8e

Strain-modulated ultrafast magneto-optic dynamics of graphene nanoflakes decorated with transition-metal atoms

Yiming Zhang(张一鸣), Jing Liu(刘景), Chun Li(李春), Wei Jin(金蔚), Georgios Lefkidis, and Wolfgang Hübner
Chin. Phys. B, 2021, 30 (**9**): 097702. DOI: 10.1088/1674-1056/abeef1

The interface density dependence of the electrical properties of $0.9Pb(Sc_{0.5}Ta_{0.5})O_3$-$0.1PbTiO_3$/$0.55Pb(Sc_{0.5}Ta_{0.5})O_3$-$0.45PbTiO_3$ multilayer thin films

Li Xue-Dong (李雪冬), Liu Hong (刘洪), Wu Jia-Gang (吴家刚), Liu Gang (刘刚), Xiao Ding-Quan (肖定全), Zhu Jian-Guo (朱建国)
Chin. Phys. B, 2015, 24 (**10**): 107701. DOI: 10.1088/1674-1056/24/10/107701

Influence of strain distribution on the morphology evolution of a Ge/GeO_2 core/shell nanoparticle confined in ultrathin Al_2O_3 thinfilm by surface oxidation

Zhang Ying (章英), Huang Hong-Hua (黄红华), Liu Xiao-Shan (刘晓山), Luo Xing-Fang (骆兴芳), Yuan Cai-Lei (袁彩雷), Ye Shuang-Li (叶双莉)
Chin. Phys. B, 2015, 24 (**3**): 037701. DOI: 10.1088/1674-1056/24/3/037701

Strain-engineered anisotropic conductance enhancement in corrugated monolayer MoS_2

Yimai Jiang(蒋伊麦), Jianing Tan(谭家宁), Meng Ge(葛蒙), and Gang Ouyang(欧阳钢)†

Key Laboratory of Low-Dimensional Quantum Structures and Quantum Control of Ministry of Education, School of Physics and Electronics, Hunan Normal University, Changsha 410081, *China*

(Received 3 August 2025; revised manuscript received 15 September 2025; accepted manuscript online 30 September 2025)

To enhance the transport properties of monolayer MoS_2 (ML-MoS_2)-based electronic devices, we systematically investigate the curvature-dependent electronic structure and carrier mobility in a corrugated ML-MoS_2 using density functional theory and the non-equilibrium Green's function method. We reveal that localized strain induces a polarized electric field, which modifies the band structure and delocalizes the electronic states, thereby significantly improving charge transport efficiency. The conductance along the zigzag direction exhibits 10^7-fold enhancement with increasing curvature. At a maximum local strain of 10%, the electronic mobility reaches 613.68 $cm^2 \cdot V^{-1} \cdot s^{-1}$, representing a 9.1-fold improvement over planar ML-MoS_2. Our results agree well with available evidence and provide crucial insights for designing high-performance devices via strain engineering.

Keywords: density functional theory, corrugated monolayer MoS_2, strain engineering, transport properties

PACS: 77.80.bn, 73.23.–b, 71.15.Mb

DOI: 10.1088/1674-1056/ae0d59 **CSTR:** 32038.14.CPB.ae0d59

1. Introduction

Two-dimensional (2D) materials, characterized by atomic-scale thickness and dangling-bond-free surfaces, exhibit exceptional capabilities in suppressing short-channel effects through quantum confinement, thereby extending the scalability of semiconductor devices under Moore's law.[1] Among these materials, molybdenum disulfide (MoS_2) has emerged as a prototypical 2D semiconductor, finding widespread applications in next-generation electronic,[2,3] ferroelectric,[4,5] and optoelectronic[6,7] devices due to its superior charge transport properties and tunable optical responses. Monolayer MoS_2 (ML-MoS_2) exhibits excellent air stability,[8] and possesses a direct band gap ($\sim$ 1.8 eV) approximately twice that of silicon, rendering it particularly advantageous for low-power transistor architectures. However, intrinsic limitations, such as low carrier mobility ($<$200 $cm^2 \cdot V^{-1} \cdot s^{-1}$ at room temperature) and high contact resistance, hinder its full performance potential in practical devices.[9,10] For instance, limited carrier mobility remains a key challenge for MoS_2-based field-effect transistors (FETs),[11] photodetectors[12] and sensors.[13]

To optimize the performance of MoS_2-based devices, researchers have employed various strategies, including contact engineering,[14–16] chemical doping,[17–19] layer thickness modulation[20] and heterostructure integration.[21,22] Among these, strain engineering has emerged as a powerful method for tailoring electrical properties.[23,24] Unlike global strain techniques, local strain engineering enables precise spatial control at the nanoscale. Experimentally, local strain can be introduced into 2D materials via pre-strained elastomers, lattice mismatch, thermal expansion coefficient (TEC) mismatch, patterned substrates, bubbles and atomic force microscope (AFM) tips.[25] This capability is particularly critical for atomically thin MoS_2, where Tang *et al.*[26] observed layer-dependent bending behavior during mechanical deformation using *in situ* microscopy and molecular dynamics simulations. Recent theoretical and experimental investigations further confirm that localized strain gradients can systematically modulate the electronic band structures of MoS_2 (e.g., direct-to-indirect bandgap transition) and charge transport properties.[27–31] However, when ML-MoS_2 undergoes nonuniform corrugation, flexoelectric polarization occurs, significantly altering carrier mobility and conductance. Understanding these strain-mediated electromechanical coupling effects is thus essential for advancing high-performance ML-MoS_2 devices.

In this study, we construct a corrugated ML-MoS_2 device with tunable curvature gradients to systematically investigate the relationship between localized strain and charge transport properties. We find that a strong anisotropic enhancement in conductance along the zigzag direction scales monotonically with curvature-induced strain. Remarkably, at a local strain of 10%, the electron mobility surges to 613.68 $cm^2 \cdot V^{-1} \cdot s^{-1}$, representing a 9.1-fold improvement over flat monolayer devices. Our findings reveal that this transport enhancement arises from strain-mediated band structure modulation, which reduces carrier effective mass and delocalizes electronic states. These re-

†Corresponding author. E-mail: gangouy@hunnu.edu.cn

© 2026 Chinese Physical Society and IOP Publishing Ltd. All rights, including for text and data mining, AI training, and similar technologies, are reserved.

sults not only quantify the strain-transport coupling in ML-MoS_2 but also establish a predictive framework for optimizing curvature-engineered 2D electronics.

2. Theoretical methodologies

All the optimizations of geometry and the electronic structure are implemented using the Vienna *ab initio* simulation package (VASP)[32,33] based on density functional theory (DFT). The exchange–correlation energy is addressed using the Perdew–Burke–Ernzerhof (PBE) function within the generalized gradient approximation (GGA).[34] The calculations were conducted using the projector-augmented plane wave (PAW) method, with a plane wave cutoff energy set to 500 eV. The optimization of the crystal cell structure was conducted with a force convergence criterion of 0.005 eV/Å, and the energy difference between two sequential steps was less than 10^{-5} eV. Brillouin-zone integration of ML-MoS_2 is performed with the $1\times6\times1$ k-point grids determined by the Monkhorst–Pack scheme.[35] In addition, a vacuum space of 30 Å is selected to prevent interactions between periodic replicas. The pre-processing and post-processing of data are performed using the VASPKIT.[36]

The electronic transport calculations were performed using the Nanodcal package, which combines DFT and non-equilibrium Green's function (NEGF).[37,38] A $1\times10\times1$ k-point grid is used in self-consistent calculations of the ML-MoS_2 device, and the k-point grid for calculating the transmission coefficient is $1\times101\times1$. The transmission for electrons incident from the left part through the device region to the right part is expressed as follows:

$$T(E,V)=\mathrm{tr}\left[\Gamma_{\mathrm{R}}(E,V)G^{\mathrm{R}}(E,V)\Gamma_{\mathrm{L}}(E,V)G^{\mathrm{A}}(E,V)\right], \quad (1)$$

where Γ and G^{A} denote the coupling matrices of the electrodes on both sides and the Green's function of the central region, respectively. The current was calculated based on the Landauer formula[39,40]

$$I(V)=\frac{2e}{h}\int_{\mu_{\mathrm{L}}}^{\mu_{\mathrm{R}}}\mathrm{d}E\left[f_{\mathrm{L}}(E-\mu_{\mathrm{L}})-f_{\mathrm{R}}(E-\mu_{\mathrm{R}})\right]T(E,V), \quad (2)$$

where V displays the applied bias voltage, $f_{\mathrm{L}}(E-\mu_{\mathrm{L}})$ and $f_{\mathrm{R}}(E-\mu_{\mathrm{R}})$ are the Fermi distribution functions of the left and right leads, with μ_{L} and μ_{R} the electrochemical potentials in the corresponding leads. Thus, the conductance (G) can be represented as

$$G=\frac{I}{(\mu_{\mathrm{L}}-\mu_{\mathrm{R}})/|e|}=\frac{2e^2}{h}T, \quad (3)$$

when using the Nanodcal package to calculate conductance, the built-in temperature is set to 0 K.

The carrier mobility is calculated by the deformation potential (DP) theory proposed by Bardeen and Shockley.[41] Based on the effective mass approximation, the carrier mobility of 2D materials can be calculated using the following formula:[41]

$$\mu=\frac{2e\hbar^3C}{3k_{\mathrm{B}}T|m^*|^2E_1^2}, \quad (4)$$

where T represents the temperature, m^* denotes the effective mass, E_1 is the DP constant, and C is the elastic modulus of the crystal. For 2D systems, the in-plane stiffness is given by $C=\left(\partial^2E/\partial\delta^2\right)/S_0$, where E is the total energy of the supercell, δ is the applied uniaxial strain, and S_0 is the area of the optimized supercell.

3. Results and discussion

Figure 1(a) illustrates the atomic structure of ML-MoS_2 with an orthogonal supercell outlined by dashed lines, where a_{o1} and a_{o2} correspond to the armchair and zigzag directions, respectively. ML-MoS_2 exhibits two distinct phases, 1T and 2H, with the 2H phase being the more stable configuration. Thus, we adopt 2H ML-MoS_2 for device construction. The smallest unit selected, shown in Fig. 1(b), consists of 24 Mo atoms and 48 S atoms. The lattice constants for flat and corrugated ML-MoS_2 are provided in Table S1. The local bending strain in ML-MoS_2 follows a sinusoidal function $x'=x+a\sin(2\pi z)$, where a represents the amplitude in fractional coordinates. Devices were constructed for both flat and corrugated MoS_2 along the zigzag (Fig. 1(c)) and armchair (Fig. S1(a)) directions.

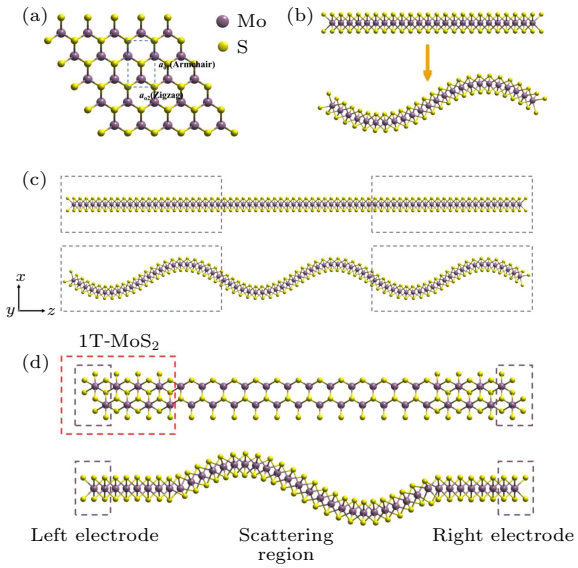


Fig. 1. (a) Atomic structure model of ML-MoS_2. Dashed lines represent the orthogonal supercell (defined by a_{o1} and a_{o2}). (b) Relaxed structures of the flat ($a=0$) and corrugated ($a=0.1$) ML-MoS_2. (c) Side views of flat and corrugated MoS_2 devices along the zigzag direction. (d) Top and side views of MoS_2 devices with 1T-MoS_2 electrodes along the zigzag direction.

For the corrugated surface, the strain (ε) is given by[42] $\varepsilon=\frac{\Delta L}{L}=\frac{R\alpha-W}{W}$, where L, ΔL, W, R and α denote the original length, length change, width, radius and arc angle of the

corrugated layer, respectively. The values of R and α can be derived from $R = \frac{d^2+(w/2)^2}{2d}$, and $\alpha = 2\arcsin\frac{(w/2)}{R}$, where w is the chord length corresponding to α, while d is the distance from the vertex to the chord, as illustrated in Fig. S1(b). According to the derivation, the strains corresponding to different amplitudes a are: 2.96% ($a = 0.06$), 5.20% ($a = 0.08$), 8.02% ($a = 0.10$) and 10% ($a = 0.115$). Notably, 2D TMDs exhibit high flexibility, enduring strains up to 10% ($a = 0.115$) before fracture.[43]

Figure 2(a) shows the conductance variation with parameter a for the armchair and zigzag directions. The results reveal anisotropic behavior in MoS_2 under local strain. This shows that the conductance increases significantly along the zigzag direction but remains nearly unchanged along the armchair direction. This anisotropy arises because strain enhances the density of states near the Fermi level and reduces the band gap in the zigzag direction, while these properties show minimal variation in the armchair direction, as illustrated in Fig. S2. Consequently, subsequent analyses focus solely on the zigzag direction. Remarkably, at $a = 0.1$, the zigzag conductance increases by approximately seven orders of magnitude compared to the flat structure ($a = 0$). Figure 2(b) presents the I–V curves for ML-MoS_2 under varying bending strains along the zigzag direction. Clearly, transport performance improves significantly with increasing local strain upon bias application.

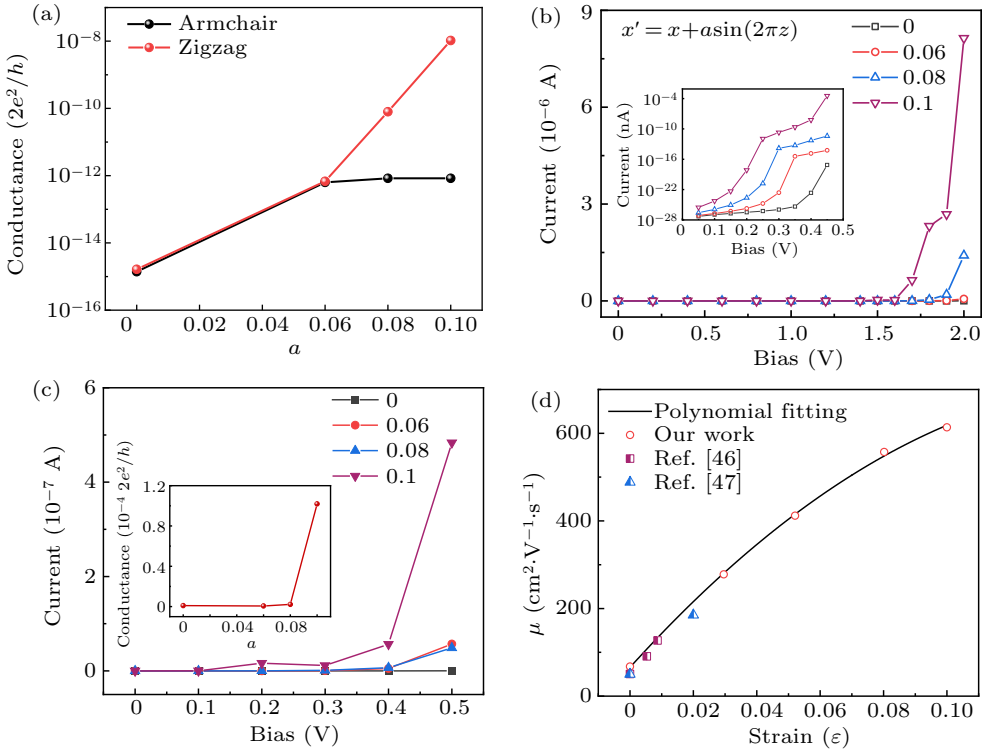


Fig. 2. (a) Conductance of ML-MoS_2 versus parameter a. Black and red lines denote the armchair and zigzag directions. I–V curves of ML-MoS_2 devices with (b) 2H- and (c) 1T-MoS_2 electrodes in the zigzag direction. Different colored lines represent varying parameters a of ML-MoS_2. Insets are the schematic diagram of I–V curves under bias voltages of 0–0.5 V (b) and the conductance of devices with 1T-MoS_2 electrodes as a function of parameter a (c). (d) Variation of μ with strain (ε) and the corresponding fitted curve.

Although local strain significantly enhances the electrical conductance of MoS_2 compared to its flat counterpart, the maximum conductance only reaches 1.05×10^{-8} $2e^2/h$. Given the relatively low conductance and current when using MoS_2 as an electrode, we employed metallic 1T-MoS_2 as the electrode material to better simulate experimental conditions, as illustrated in Fig. 1(d). This choice serves as an efficient buffer layer to reduce central scattering effects while maintaining excellent lattice matching between the two crystallographic phases. The conductance and I–V characteristics for devices with 1T-MoS_2 electrodes were also calculated, as shown in Fig. 2(c). The trends closely resemble those observed in 2H-MoS_2 electrode devices, but with a dramatic increase in conductance from 9.67×10^{-7} $2e^2/h$ ($a = 0$) to 1.02×10^{-4} $2e^2/h$ ($a = 0.1$). Moreover, at a bias of just 0.5 V, the current reaches 10^{-7} A, consistent with values reported by other studies.[44,45] To ensure computational reliability, we performed a k-point convergence test for conductivity along the periodic direction of the device, as shown in Fig. S3. The results confirm that the conductivity converges with increasing k-point density, and the selected $1 \times 100 \times 1$ grid is sufficient for accurate calculations.

For quantitative analysis, we calculated the elastic modulus, deformation potential (DP) constant, and effective mass of corrugated MoS_2. Using Eq. (4), we derived the carrier mobility, with the results summarized in Fig. S4 and Table 1. A

polynomial fit reveals the strain (ε)-dependent electron mobility, $\mu = -a\varepsilon^2 + b\varepsilon + c$, where $a = -35579.3$, $b = 9148.3$ and $c = 61.6$, aligning well with experimental data,[46,47] as illustrated in Fig. 2(d). Notably, the mobility increases nonlinearly with strain, but the enhancement rate diminishes at higher strains due to finite electronic state delocalization. For comparison, we evaluated mobility under in-plane biaxial strain,[24,48] as shown in Fig. S5. Strikingly, local strain induces a more pronounced mobility enhancement than biaxial strain, consistent with experimental observations.

Table 1. Strain (ε), band gap (E_g), elastic modulus (C), DP constant (E), electron effective mass (m_e) and electronic mobility (μ) along the transport direction in ML-MoS_2 with different a.

a	ε	E_g (eV)	C (N/m)	E (eV)	m_e	μ ($cm^2 \cdot V^{-1} \cdot s^{-1}$)
0	0	1.661 (dir.)	124.34	–11.02	0.451	67.48
0.06	2.96%	1.356 (ind.)	124.34	–5.60	0.414	277.89
0.08	5.20%	0.144 (ind.)	124.34	–5.03	0.398	441.97
0.10	8.02%	0.908 (ind.)	124.34	–4.50	0.396	557.31
0.115	10%	0.739 (ind.)	124.34	–4.08	0.416	613.68

To investigate how local strain affects transport properties, we performed Bader charge analysis on corrugated MoS_2 (Fig. 3(a)), quantifying charge transfer relative to the flat structure at $a = 0.1$. Local strain breaks structural symmetry, inducing electron transfer from the inner curve (valley) to the outer curve (peak). This occurs because mechanical bending elongates Mo-S bonds in the peak region (tensile strain) while shortening them in the valley (compressive strain), leading to charge redistribution towards the tensile-strained areas. As the curvature increases, the charge redistribution becomes more pronounced, causing electron accumulation in the S atomic layers at the peak, where tensile strain is maximized. This creates a polarization electric field perpendicular to the transport direction, facilitating electron–hole pair separation. In addition, the valence band maxima (VBM) wave functions for zigzag-aligned ML-MoS_2 (Figs. 3(b) and S6) show uniform in-plane distribution in the unstrained case. Under strain gradients, however, wave function overlap and bonding characteristics emerge in the peak region. With increasing strain, the wave functions delocalize, directly enhancing conductance.

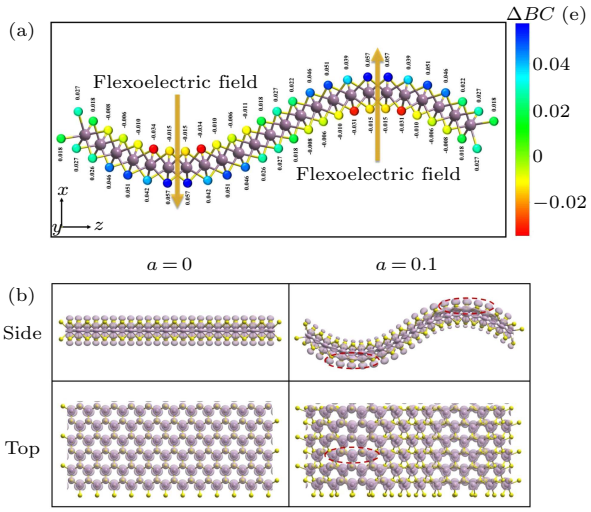


Fig. 3. (a) Bader charge transfer in corrugated ($a = 0.1$) ML-MoS_2 with respect to flat ($a = 0$) ML-MoS_2. Color indicates the extent of charge transfer. (b) Top and side views of ML-MoS_2 wave function correspond to the valence band maxima at $a = 0$ (flat) and 0.1, respectively.

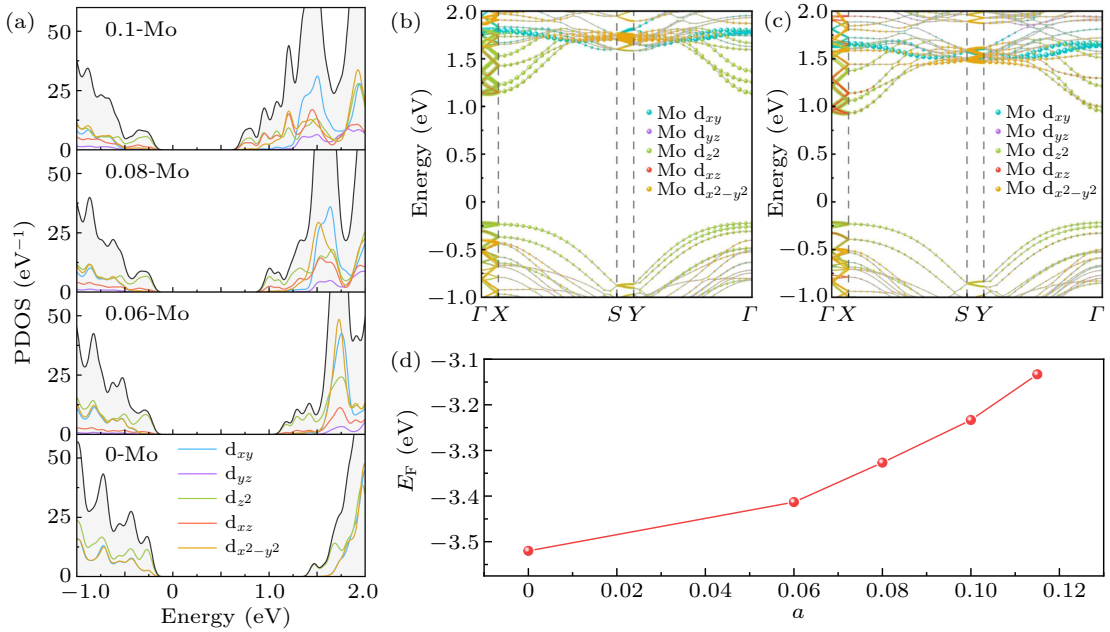


Fig. 4. (a) PDOS for MoS_2 supercell at different parameters a. Effects of local strain on the electronic structure of ML-MoS_2 for $a = 0$ (flat) (b) and $a = 0.1$ (c) cases. Orbital projected eigenvalues are represented by different colors. (d) Fermi energy varies with parameters a under local strain.

Generally, strain-driven structural relaxation alters bond lengths and angles, modulating orbital coupling strengths and band gaps.[49–51] Figure 4(a) shows the projected density of states (PDOS) for Mo atoms in ML-MoS_2 under strain. Obviously, in flat MoS_2, the conduction band minimum (CBM) and VBM arise primarily from p orbitals of S atom and d_{xy} (blue), d_{z^2} (green) and $d_{x^2-y^2}$ (yellow) orbitals of Mo atom. The d_{xz} and d_{yz} orbitals (red) contribute minimally due to strong coupling between p orbitals of S atoms and $d_{xz}+d_{yz}$ orbitals of Mo atoms, which splits bonding and antibonding states. Local strain reduces crystal symmetry from D_{3h} to C_1, lifting degeneracy between d_{xy} and $d_{x^2-y^2}$ orbitals, as well as d_{xz} and d_{yz} orbitals. Projected band structures under various curvatures are shown in Figs. 4(b) and 4(c) as well as in Figs. S7(a) and S7(b). Notably, flat MoS_2 exhibits a direct band gap of 1.661 eV, with both the VBM and CBM located at the Γ point of the first Brillouin zone. Upon the application of local strain, the direct band gap transitions to an indirect type, accompanied by a gradual reduction as the strain increases. At the maximum curvature limit, the band gap reaches 0.739 eV when $a = 0.115$. The corresponding bandgap values for different degrees of curvature are presented in Table 1. Concurrently, compared to the unstrained state, strain induces an upward shift of the Fermi level (Fig. 4(d)), a phenomenon also confirmed in other periodic structures.[52,53] Therefore, these effects, including bandgap narrowing and barrier reduction significantly enhance the transport properties of ML-MoS_2.

4. Conclusion

In summary, we systematically investigate the transverse flexoelectric and charge transport properties of corrugated ML-MoS_2 using DFT and the NEGF method. Our results demonstrate that localized strain induces a significant enhancement of transport properties along the zigzag direction, with electron mobility following a characteristic curvature-dependent relationship, $\mu = -35579.3\varepsilon^2 + 9148.3\varepsilon + 61.6$. This improvement stems from strain-gradient-mediated electronic structure modulation, which reduces the band gap and promotes delocalization of electronic states, thereby optimizing charge transport in ML-MoS_2 devices. Through detailed analysis of the effective mass and mobility variations under strain, this study provides fundamental insights for the rational design of high-performance MoS_2-based electronic devices via strain engineering.

Acknowledgement

This study was supported by the National Natural Science Foundation of China (Grant No. 12474226).

References

[1] Chhowalla M, Jena D and Zhang H 2016 *Nat. Rev. Mater.* **1** 16052
[2] Jayachandran D, Pendurthi R, Sadaf M U K, Sakib N U, Pannone A, Chen C, Han Y, Trainor N, Kumari S, Mc Knight T V, Redwing J M, Yang Y and Das S 2024 *Nature* **625** 276
[3] Yu L, Mi M, Wang S, Fan Q, Xiao H, Zhang Y, Lyu B, Liu M, Wang S and Wang Y 2024 *Appl. Phys. Lett.* **124** 122108
[4] Bian R, He R, Pan E, Li Z, Cao G, Meng P, Chen J, Liu Q, Zhong Z, Li W and Liu F 2024 *Science* **385** 57
[5] Tsang C S, Zheng X, Yang T, Yan Z, Han W, Wong L W, Liu H, Gao S, Leung K H, Lee C S, Lau S P, Yang M, Zhao J and Ly T H 2024 *Science* **386** 198
[6] Lee M, Hong H, Yu J, Mujid F, Ye A, Liang C and Park J 2023 *Science* **381** 648
[7] Maity D, Sharma R, Sahoo K R, Lal A, Arenal R and Narayanan T N 2024 *Phys. Rev. Mater.* **8** 084002
[8] Mirabelli G, McGeough C, Schmidt M, McCarthy E K, Monaghan S, Povey I M, McCarthy M, Gity F, Nagle R, Hughes G, Cafolla A, Hurley P K and Duffy R 2016 *J. Appl. Phys.* **120** 125102
[9] Radisavljevic B, Radenovic A, Brivio J, Giacometti V and Kis A 2011 *Nat. Nanotechnol.* **6** 147
[10] Kang J, Liu W, Sarkar D, Jena D and Banerjee K 2014 *Phys. Rev. X* **4** 031005
[11] Liu H, Neal A T and Ye P D 2012 *ACS Nano* **6** 8563
[12] Chen R, Pei Y, Kang Y, Liu J, Xia Y, Wang J, Xu H, Jiang C, Li W and Xiao X 2022 *Adv. Electron. Mater.* **8** 2200281
[13] Kumar R, Goel N, Hojamberdiev M and Kumar M 2020 *Sens. Actuators Phys.* **303** 111875
[14] Das S, Chen H Y, Penumatcha A V and Appenzeller J 2013 *Nano Lett.* **13** 100
[15] English C D, Shine G, Dorgan V E, Saraswat K C and Pop E 2016 *Nano Lett.* **16** 3824
[16] Zhang S, Le S T, Richter C A and Hacker A 2019 *Appl. Phys. Lett.* **115** 073106
[17] Lin L, Guo Y, He C Z, Tao H L, Huang J, Yu W, Chen R, Lou M and Yan L 2020 *Chin. Phys. B* **29** 097102
[18] Zhang L, Wang G, Zhang Y, Cao Z, Wang Y, Cao T, Wang C, Cheng B, Zhang W, Wan X, Lin J, Liang S J and Miao F 2020 *ACS Nano* **14** 1026
[19] Torsi R, Munson K T, Pendurthi R, Marques E, Van Troeye B, Huberich L, Schuler B, Feidler M, Wang K, Pourtois G, Das S, Asbury J B, Lin Y C and Robinson J A 2023 *ACS Nano* **17** 156295
[20] Lee H, Deshmukh S, Wen J, Costa V Z, Schuder J S, Sanchez M, Ichimura A S, Pop E, Wang B and Newaz A K M 2019 *ACS Appl. Mater. Interfaces* **11** 31543
[21] Wang C, Cusin L, Ma C, Unsal E, Wang H, Consolaro V G, Montes García V, Han B, Vitale S, Dianat A, Croy A, Zhang H, Gutierrez R, Cuniberti G, Liu Z, Chi L, Ciesielski A and Samorì P 2023 *Adv. Mater.* **36** 2305882
[22] Zhang Y, Wang L, Bian Q, Zhong C, Chen Y and Jiang L 2024 *Small* **20** 2311379
[23] Harada N, Sato S and Yokoyama N 2014 *J. Appl. Phys.* **115** 034505
[24] Hosseini M, Elahi M, Pourfath M and Esseni D 2015 *IEEE Trans. Electron Devices* **62** 3192
[25] Wang J, He L, Zhang Y, Nong H, Li S, Wu Q, Tan J and Liu B 2024 *Adv. Mater.* **36** 2314145
[26] Tang D M, Kvashnin D G, Najmaei S, Bando Y, Kimoto K, Koskinen P, Ajayan P M, Yakobson B I, Sorokin P B, Lou J and Golberg D 2014 *Nat. Commun.* **5** 3631
[27] Chang H Y, Yang S, Lee J, Tao L, Hwang W S, Jena D, Lu N and Akinwande D 2013 *ACS Nano* **7** 5446
[28] Liu T, Liu S, Tu K H, Schmidt H, Chu L, Xiang D, Martin J, Eda G, Ross C A and Garaj S 2019 *Nat. Nanotechnol.* **14** 223
[29] Ng H K, Xiang D, Suwardi A, Hu G, Yang K, Zhao Y, Liu T, Cao Z, Liu H, Li S, Cao J, Zhu Q, Dong Z, Tan C K I, Chi D, Qiu C, Hippalgaonkar K, Eda G, Yang M and Wu J 2022 *Nat. Electron.* **5** 489
[30] Shevliakova H V, Yesylevskyy S O, Kupchak I, Dovbeshko G I, Kim Y and Morozovska A N 2021 *Symmetry* **13** 2086
[31] Qi J, Li X, Qian X and Feng J 2013 *Appl. Phys. Lett.* **102** 173112
[32] Kresse G and Furthmüller J 1996 *Phys. Rev. B* **54** 11169
[33] Kresse G and Furthmüller J 1996 *Comput. Mater. Sci.* **6** 15
[34] Perdew J P, Burke K and Ernzerhof M 1996 *Phys. Rev. Lett.* **77** 3865
[35] Monkhorst H J and Pack J D 1976 *Phys. Rev. B* **13** 5188

[36] Wang V, Xu N, Liu J C, Tang G and Geng W T 2021 *Comput. Phys. Commun.* **267** 108033
[37] Taylor J, Guo H and Wang J 2001 *Phys. Rev. B* **63** 245407
[38] Taylor J, Guo H and Wang J 2001 *Phys. Rev. B* **63** 121104
[39] Landauer R 1970 *Philos. Mag.* **21** 863
[40] Büttiker M 1986 *Phys. Rev. Lett.* **57** 1761
[41] Bardeen J and Shockley W 1950 *Phys. Rev.* **80** 72
[42] Kang S, Jeon S, Kim S, Seol D, Yang H, Lee J and Kim Y 2018 *ACS Appl. Mater. Interfaces* **10** 27424
[43] Bertolazzi S, Brivio J and Kis A 2011 *ACS Nano* **5** 9703
[44] John A P, Thenapparambil A and Thalakulam M 2020 *Nanotechnology* **31** 275703
[45] Wu G, Lou H, Liu K and Lin X 2020 *Phys. Chem. Chem. Phys.* **22** 21888
[46] Chen Y, Lu D, Kong L, Tao Q, Ma L, Liu L, Lu Z, Li Z, Wu R, Duan X, Liao L and Liu Y 2023 *ACS Nano* **17** 14954
[47] Liu X 2024 *Nat. Commun.* **15** 6934
[48] Du G, Li C and Cheng L 2023 *Phys. Rev. B* **107** 085422
[49] Chang C H, Fan X, Lin S H and Kuo J L 2013 *Phys. Rev. B* **88** 195420
[50] Wang Y, Ge M, Tan J, Cai B and Ouyang G 2025 *Sci China Inf. Sci.* **68** 159402
[51] Dong J and Ouyang G 2020 *Chin. Phys. B* **29** 086403
[52] Yu L, Ruzsinszky A and Perdew J P 2016 *Nano Lett.* **16** 2444
[53] Zheng J D and Zhao Y F 2022 *2D Mater.* **9** 035005